

Cite this: DOI: 00.0000/xxxxxxxxxx

Scalable Hybrid Deep Neural Networks/Polarizable Potentials Biomolecular Simulations including Long-range Effects[†]

Théo Jaffrelot Inizan,^a Thomas Plé,^a Olivier Adjoua,^a Pengyu Ren,^b Hatice Gökcan,^c Olexandr Isayev,^c Louis Lagardère,^{a,d} and Jean-Philip Piquemal^{a,b*}

Received Date

Accepted Date

DOI: 00.0000/xxxxxxxxxx

We present Deep-HP, a scalable multi-GPUs simulation platform dedicated to machine learning potentials. As part of the Tinker-HP molecular dynamics (MD) package, it allows users to efficiently use their Pytorch/TensorFlow Deep Neural Networks (DNNs) models (ANI, DeePMD ...) to perform MD simulations up to million-atoms systems. Thanks to its MPI multi-GPUs setup inherited from Tinker-HP, Deep-HP extends DNNs simulation timescales while offering the possibility of coupling them to any classical (FFs) and many-body polarizable (PFFs) force fields. Towards biophysical applications, we present a novel hybrid molecular dynamics simulation protocol coupling the AMOEBA PFF to the ANI-2x DNN where solvent-solvent and solvent-solute interactions are computed using AMOEBA while the solute-solute interactions are computed by ANI-2x. The strategy allows for the explicit inclusion of physical long-range effects such as multipolar electrostatics and many-body polarization via efficient periodic boundary conditions. The DNNs/PFFs partition can be user-defined allowing for hybrid simulations to include biosimulation key ingredients such as polarizable solvents, and polarizable counter-ions. To reduce the DNN computational performance gap compared to FFs, we rely on extensive multiple time stepping and focus on the models contributions to low frequency modes of nuclear forces. Therefore, the approach primarily evaluates the AMOEBA forces while including the ANI-2x ones only via a correction step resulting in an overall 20-fold acceleration over standard Velocity Verlet integration. Thanks to this approach, accessing μ s simulations with hybrid DNN/PFF models becomes possible. This allowed us to evaluate the accuracy of the ANI-2x/AMOEBA model by calculating the solvation free energies of various ligands in four different solvents, and the binding free energies of 13 challenging ligand-protein complexes. The hybrid approach is shown to be accurate even for charged ligands. Overall, the hybrid approach can outperform AMOEBA for solvation free energies in non-aqueous solvent and ligand binding free energies. This opens further perspectives for large scale hybrid DNN/PFF simulations towards biophysical applications. The Deep-HP platform will also help to foster the development of next generation of DNN models able to capture both short-range quantum accuracy and long-range physical/many-body effects.

1 Introduction

Understanding the dynamics of biological systems is a key ingredient in structural biology and drug discovery. Over the last 50 years, coupled to force fields, molecular dynamics (MD) simulations have proven to be an essential theoretical tool to pre-

^a Sorbonne Université, Laboratoire de Chimie Théorique, UMR 7616 CNRS, 75005, Paris, France

^b University of Texas at Austin, Department of Biomedical Engineering, Austin, Texas, USA

^c Carnegie Mellon University, Department of Chemistry, Pittsburgh, Pennsylvania, USA.

^d Sorbonne Université, Institut Parisien de Chimie Physique et Théorique, FR 2622 CNRS, Paris, France

Contact: jean-philip.piquemal@sorbonne-universite.fr

[†] Electronic Supplementary Information (ESI) available: See DOI:

00.0000/00000000.

dict the long-timescale behaviour of proteins in complex environments. In recent years, deep learning technologies have also progressed and showed some potential to accelerate drugs discovery. For example, in the last months, DeepMind developed the AlphaFold²¹ model that is able to predict over 200 million protein structures. Proteins' properties could, however, drastically change during a molecular dynamics simulation. For instance, the protein-water interface can drive fluctuations of catalytic cavities and thus change drug inhibition. MD is therefore the prominent approach to go beyond simple structure in order to predict the complete protein conformational space.²⁻⁴ Due to the biological system sizes and biological simulation timescales, pure quantum chemistry models cannot be used for simulations and are replaced by empirical force fields (FFs), that are presently commonly used to model chemical interactions.

FFs model the total energy as a sum over intra and intermolecular energy terms. The treatment of the latter leads to two classes of FFs: classical and polarizable. In classical FFs, the intermolecular interactions are modeled by Lennard-Jones and Coulomb potential which make them computationally efficient at, sometimes, the expense of accuracy. While offering an acceptable precision thanks to careful parametrizations, they lack an accurate description of polarization and to a larger extent of many-body physical effects.^{5,6} These quantities can play a crucial role in solvation and for the stability of secondary, and quaternary structures of proteins.⁷ The development of polarizable FFs (PFFs) has opened new routes able to explicitly include many-body effects.^{8,9} Their computational cost has long hindered their use but with the rise of High Performance Computing (HPC) and the increasing performance of computational devices such as *GPUs*, million-atoms PFFs simulations can be now considered as routine.^{2,10,11}

At this stage, Machine Learning (ML) schemes have also the potential to offer a new paradigm for boosting MD simulations and to take their part in the development of FFs. ML potentials (MLP) also avoid solving the Schrödinger equation at each time-step of the simulation by providing a mathematical direct relation between the atomic positions and the potential energy. In recent years, MLPs have been an active field of research which led to the emergence of different framework such as high-dimensional deep neural network potentials (HDNNPs), Gaussian approximation potentials (GAP),¹² moment tensor potentials, spectral neighbor analysis potentials (SNAP),¹³ atomic cluster expansion, graph networks, kernel ridge regression methods,¹⁴ gradient-domain machine learning (GDML)¹⁵⁻¹⁸ and support vector machines (SVM).¹⁹ MLP nonlinear functional forms are very general and highly flexible, allowing for a very accurate representation of electronic structure computations reference data. The input of a MLP is usually a hand-crafted real valued functions of the coordinates that preserve some symmetries and uniquely defined atomic environments. In practice, the choice of this descriptor is central to design an accurate MLP. A variety of physics-based descrip-

tor have been developed such as the smooth overlap of atomic positions (SOAP),²⁰ the spectrum of approximated Hamiltonian matrices representations (SPAHM),²¹ the Coulomb matrix (CM) and the atom-centered symmetry functions (ACSFs).^{22,23} The latter, introduced by Behler and Parinello in 2007, is still the most popular descriptor used for HDNNP and have been employed in numerous studies.^{22,24} It describes the atomic environment of a given central atom inside a cutoff radius R_c by the use of radial and angular functions. Some modifications of the initial symmetry functions have been done since, aiming to reduce the number of symmetry functions that exhibit quadratic growth with the number of elements or improve the probing of the atomic environment²⁵. However, even if such descriptor have considerably improved the transferability and the scalability of HDNNPs, they are often use to only study "small" chemical systems that remain far away from the needs of biological modeling. Another issue has been the lack of efficient MLP multi-GPU infrastructure software inside an already existing molecular dynamics package. In the last couple of years things started to change and our work is part of this large movement and also aims to address recent development of the ML-field.²⁶ While our work aims to utilize new developments in ML-field, we also aim to address some of the shortcomings of MLPs.

Indeed, the intrinsic architecture of MLP usually constrains them to short-range interactions. Recently, Tsz Wai Ko *et al.* proposed a fourth-generation of HDNNP which is able to capture long-range charge transfer and multiple charge states.²⁷ While it demonstrates the power of ML, their computational cost is much higher compared to physics-based PFFs long-range models and is not able to correctly describe solute in water.

To address these challenges, we present Deep-HP, a multi-GPU MLP platform which is part of the Tinker-HP package and enables the coupling and development of MLP with state-of-the-art many-body polarizable effects.

Tinker-HP uses massive parallelization by means of 3D decomposition which is a particularly well suited strategy for MLPs that are often developed by decomposing the total energy as a sum of atomic energy contributions.^{10,11} The platform theoretical scalability with MLPs is linear and allows to scale up to thousands of *GPUs*. As the present code shares the Tinker-HP capabilities, it allows for invoking fast physics-based many-body energy contributions. We extensively test Deep-HP scalability and implementation on the ANI model, one of the most accurate MLPs up to date for small organic molecules. Finally, we describe a hybrid PFFs-ANI model that uses ANI to model solute-solute interactions and AMOEBA for solvent-solute as well as solvent-solvent interactions. This enables the ANI neural network coupling with the AMOEBA capabilities such as its accurate water model, counterions and long-range/many-body interactions. As AMOEBA handles polarization and solute-solvent interactions, it increases ANI transferability to a broader range of systems including charged

ones. The performance of the model is evaluated by calculating the solvation free energies of 80 molecules in four common organic solvents as well as the binding free energies of 13 host-guest complexes, showing high accuracy w.r.t experiment.

2 Potential Energy Models

2.1 The AMOEBA Polarizable Force Field

The total potential energy of the AMOEBA^{28,29} polarizable model is expressed as the sum of bonded and non-bonded energy terms:

$$\begin{aligned} E_{total} &= E_{bonded} + E_{nonbonded} \\ E_{bonded} &= E_{bond} + E_{angle} + E_{b\theta} \\ E_{nonbonded} &= E_{vdW} + E_{ele}^{perm} + E_{ele}^{pol} \end{aligned} \quad (1)$$

The bonded terms embody MM3-like³⁰ anharmonic bond-stretching and angle-bending terms. Regarding the specific case of the polarizable AMOEBA water model, the intramolecular geometry and vibrations are described with an Urey-Bradley approach.²⁸

The non-bonded terms include the van der Waals (vdW) interactions and the electrostatic contributions from both permanent and induced dipoles (polarization). More precisely, the polarization contribution is computed using an Applequist/Thole model³¹ whereas Halgren’s buffered 14-7 pair potential is used to model vdW interactions.³² Computing the polarization energy requires the resolution of a linear system to get the induced dipoles, which is made through the use of iterative solvers such as preconditioned conjugated gradient that is the one used in this paper (with a 1×10^{-5} tolerance).¹¹

To model the electrostatic interactions, AMOEBA relies on point atomic multipoles truncated at the quadrupole level. More details about the functional form and parametrization of AMOEBA can be found in reference.³³ Electrostatics and many-body polarization long-range interactions are fully included through the use of the Smooth Particle Mesh Ewald approach^{34,35} that allows for periodic boundary conditions simulations. Besides water²⁸, AMOEBA is a general force field available for many solvent³⁶, ions,^{37,38} proteins³⁹ and nucleic acids⁴⁰ biomolecular simulations.

2.2 Neural Network Potentials

Feed-forward neural network (FFNN) is a machine learning model that uses as building blocks connected layers of nodes (i.e neurons) each associated with their weights and bias. The output of each neuron is computed through a function of the output of the previous layer. Each weight is the strength associated to a specific node connection and they are updated during the training process. The depth (i.e number of layers) of the FFNN is related to its flexibility and the complexity of the training dataset. Through careful optimization of hyperparameters, weights, biases and ar-

chitecture, the FFNN can learn high dimensional non-linear functions such as potential energy surfaces (PESs). For HDNNP, the FFNN maps molecular structures to potential energy. The original HDNNP, introduced by Behler and Parrinello, expresses the total energy of a system E_T as a sum of atomic contributions E_i .

$$E_T = \sum_i^{N_{atoms}} E_i(G_i) \quad (2)$$

where G_i is the atomic environment vector (AEV) of atom i . Based on the assumption of locality, each atom i is associated with an AEV which probes specific radial and angular chemical regions. Each G_i is then used as input into a single HDNNP. The construction of AEVs for each atom in the system enable the use of models for large systems even though they are trained on small molecules. Moreover, this summation has the advantage that it scales linearly with respect to the number of atoms. This atomic decomposition scheme has notably accelerated the development of HDNNP with increasingly complex architectures and AEV schemes.

2.3 ANI models

Smith et al. developed ANI, a model that uses a modified version of the Behler-Parinello symmetry functions (BPSFs).^{25,41} Symmetry functions are building blocks of the so called atomic environment vector (AEV), $G_i = \{G_1^X, \dots, G_M^X\}$, which aims to probe angular and radial local environment of a central atom i with atomic number X . The locality approximation is achieved by using a differentiable cutoff function:

$$f_c(R_{ij}) = \begin{cases} 0 & R_{ij} > R_c \\ \frac{1}{2} \cos\left\{\frac{\pi R_{ij}}{R_c}\right\} + 0.5 & R_{ij} \leq R_c \end{cases} \quad (3)$$

where R_{ij} is the distance between the central atom i and a neighbor j , and R_c a cutoff radius, here fixed to 5.2 Å. To probe the neighboring environment of the central atom inside the cutoff sphere, the AEV is divided into two types of symmetry functions: radial and angular.

The commonly used radial function is a sum of products of Gaussian and cutoff functions as introduced by Behler-Parinello:

$$G_{i,m}^{rad} = \sum_{\substack{j \neq i \\ R_{ij} \in R_c}}^{N_{atoms} \in R_c} e^{-\eta(R_{ij}-R_s)^2} f_c(R_{ij}) \quad (4)$$

The index m is associated to a set of parameters $\{\eta, R_s\}$, where R_s is the distance from the central atom for which the center of the Gaussian is shifted and η is the spatial extension of the Gaussian. The radial symmetry functions are not sufficient to distinguish between chemical environment, e.g if the neighboring atoms are all at the same distance from atom i . This is solved by using

angular symmetry functions,

$$G_{ANI-ang}^{i,m} = 2^{1-\xi} \sum_{j,k \neq i}^{N_{atoms}} (1 + \cos(\theta_{ijk} - \theta_s))^\xi e^{-\eta \left(\frac{R_{ij} + R_{ik}}{2} - R_s \right)^2} f_c(R_{ij}) f_c(R_{ik}) \quad (5)$$

where θ_{ijk} is the angle between the central atom i and neighbors j and k , θ_s used to center the maxima of the cosine and ξ changes the width of the peak. To differentiate between atom species, ANI supplied a radial part for each atomic number and an angular part for each corresponding pair inside the cutoff sphere R_c . Thus, for N atom species, the AEV has N radial and $\frac{N(N+1)}{2}$ angular sub-AEVs.

The first ANI potential, ANI-1x^{42,43}, has been developed for simulating organic molecules containing H, C, N, and O chemical elements. The recent extension to ANI, ANI-2x⁴⁴, has been trained to three additional chemical elements (S, F, and Cl). This model extends the capabilities of ANI towards more diverse chemical structures such as proteins that often contain Sulfur and Chlorine atoms.⁴⁴

As ANI remains mainly designed to study the dynamics of small-to medium-size organic molecules, it had not been initially coupled to a massively parallel infrastructure. In contrast, another popular MLP, introduced by Weinan et al.^{45,46}, DeePMD has been pushed towards large scale simulations of millions of atoms but has been trained on some specific systems, limiting its transferability.

2.4 DeePMD Models

The specificity of DeePMD compared to other MLPs is that it does not use hand-crafted symmetry functions to get the atomic environment^{45,46}.

For an atom i , its j neighbors within a cutoff radius are first sorted according to their chemical species and their inverse distances to the central atom.

The central atom is then associated to its local frame (e_x, e_y, e_z) and the local coordinates of its neighbors is denoted (x_{ij}, y_{ij}, z_{ij}). The atom i local environment $\{D_{ij}\}$ is then defined as:

$$\{D_{ij}\} = \left\{ \frac{1}{R_{ij}}, \frac{x_{ij}}{R_{ij}}, \frac{y_{ij}}{R_{ij}}, \frac{z_{ij}}{R_{ij}} \right\} \quad (6)$$

$\{D_{ij}\}$ is then used as input for a FFNN to predict the atomic energy E_i .

DeePMD has been recently pushed in order to simulate tens of millions atoms for water and copper using a highly optimized GPU code on the Summit supercomputer²⁶ but it would hugely benefit from all the available feature of Tinker-HP in order to run large scale biological simulations.

2.5 Hybrid Model: Neural Network Solutes in AMOEBA Polarizable Solvent

In local MLP models such as ANI and DeePMD, each atom only interacts with its closest neighbors within a relatively small cut-off radius. It is however well known that a correct description of long-range interactions is crucial for the simulation of condensed-phase systems, making them particularly challenging for MLP models⁴⁷. On the other hand, particular attention has been paid during the AMOEBA parametrization to accurately reproduce properties of solvents (and in particular of liquid water). It is then very attractive to combine both models in order to gain the flexibility of the ML potential while keeping the robustness of AMOEBA solvents. This can be achieved by writing the total potential energy of the so-called hybrid model as

$$\begin{aligned} V_{HYB}(P \cup W) &= V_{AMOEB A}(P \cup W) + V_{ML}(P) - V_{AMOEB A}(P) \\ &= V_{AMOEB A}(W) + V_{AMOEB A}(P \cap W) + V_{ML}(P) \end{aligned} \quad (7)$$

where P indicates the solute, W indicates the solvent, $P \cap W$ indicates the solute-solvent interactions and $P \cup W$ indicates the total system. The many-body nature of the polarization energy prevents us from directly computing $V_{AMOEB A}(P \cap W)$. To embed the ML potential, we subtract the AMOEBA potential of the isolated solute to the full AMOEBA potential. As indicated in Eq. (7), this is essentially equivalent to using AMOEBA for the solvent-solvent and solvent-solute interactions and the ML model for the solute-solute interactions. The atomic environments that are given to the ML potential therefore only comprise atoms from the solute and should be similar to data present in the training set, thus reducing occurrences of extrapolation. This coupling with AMOEBA allows to simulate atom types not available with MLPs, such as counter ions that are crucial in biology. It also enables the use of the very accurate AMOEBA water model for which current MLPs are deficient.

3 Deep-HP: A Multi-GPU MLP platform within Tinker-HP

3.1 A General Machine Learning Platform

New ML architectures are introduced daily and dedicated machine learning libraries PyTorch, TensorFlow and Keras, have created a large community of developers and users.⁴⁸⁻⁵⁰

Conversely, most of the MD codes (CHARMM, GROMACS, Tinker-HP, ...), are often written using compiled languages such as Fortran or C/C++. To allow for the simultaneous execution of both Python-based MLP codes and Tinker-HP we implemented an interface that allows for efficient data exchanges between environments while maintaining Tinker-HP as the master process which, punctually, calls the MLP code. Identified by Tinker-HP as another computational subroutine, the MLP code should be therefore provided as a Python API. We have implemented such func-

tionality using the C Foreign Function Interface (Cffi) for Python which allows for efficient API embedding, within a dynamic library (DLL) to be linked with. Technically, within such a framework we can now call Python frozen codes from C using such cffi embedding feature, thus enabling the use of various MLP codes within Tinker-HP.

In that context, the recent GPU-accelerated version of Tinker-HP¹¹ offers the opportunity to build an overall very efficient hybrid MD/MLP code as both applications are running on the same GPU platform. To do so, we need to design a Python/C interface in a way that avoids any substantial data transfers between Python and C environments. In practice, the cffi module is not natively designed to interface data structures from device memory: its dictionary can only process host addresses on array datatype or scalar data structures. Based on these constraints, our code would be forced to perform two host-device data transfers in order to communicate through Fortran/C and Python interface. To overcome this issue that would be detrimental to the global performance, we directly send generic memory addresses through the interface as scalar values and use the PyCUDA python module to manually cast these addresses into Tensor type that can actually be used by MLP codes. Fortunately, PyCUDA and PyTorch provide such casting routines. Thus, calling Python codes from Fortran/C with device data among the calling arguments can be done independently of the size of those arguments.

Furthermore, we built the interface of the MLP code in order to keep Tinker-HP model-agnostic. In practice, Tinker-HP provides positions and neighbor lists and gets energies and forces in return. Adding a new MLP to the platform then becomes an easy task, especially if it was developed using the PyTorch or TensorFlow libraries. Moreover, we implemented an API within TorchANI which allows to save and reconstruct ANI-like models using JSON, YAML and PKL formats. This allows to directly use models trained with TorchANI with the Deep-HP platform, thus reducing the hassle of transferring a model from the training stage to production simulations.

3.2 Massive Parallelism within Tinker-HP: Scalable Neural Networks Simulations

Regarding parallelism, Tinker-HP uses a three dimensional domain decomposition (DD) scheme. The simulation box is decomposed into a certain number of domains matching the exact number of parallel processes at our disposal so that each process - attached or not to a device - is assigned to a unique domain. Then, each process computes partial forces on the local atoms, communicates the partial data to his spatial neighbors, sums the partial forces and integrates the equations of motions for local atoms at each time-step. The DD method is valid and effective under the assumption that all interactions are short-range and the atomic positions do not move much between two time-steps. The same structure has been used during the development of the acceler-

ated multi-GPU version.¹¹ Naturally, we wanted to preserve this property with the MLP code interface despite the fact that TorchANI is not designed to run on multiple GPUs. Using the DD method from Tinker-HP, we can isolate the local atoms of a domain and its neighbors and send the information to a MLP code instance through the interface for calculation. We also bypass the implemented neighbor list within TorchANI, and use the one of Tinker-HP. Indeed, we verified that the TorchANI neighbor list algorithm scales as $\mathcal{O}(N^2)$ (N being the number of atoms), both in execution time and memory; which limits its applicability to small systems. For instance, a 12000 atoms water box on a Quadro GV100 GPU card supported by 32 GB of memory already caused a memory overflow. Because TorchANI requires a pair list of indices as a data structure, we adapted the highly GPU-optimized linked-cell method, thoroughly described in ref.¹¹. In practice, the list is built by partitioning the box into smaller ones and resort to an adjacency matrix and a filtering process. Finally, the complexity of the neighbor list generation outperforms the original TorchANI implementation, thus significantly reducing both the computational cost and memory footprint and allowing to handle much larger systems. For example, systems made of more than 100000 atoms are now manageable on a single 32 GB GV100 GPU. On top of that, we also noticed a constant memory allocation from Python (especially when running in parallel) which happens to be detrimental to performance and, on some occasions, can lead to a crash. This issue has been solved by resorting to an upstream bounded buffer reservation which size is proportional to the number of atoms in the system. In the end, Deep-HP is able to perform simulations of several million atoms systems, as illustrated in Figure 1 where we show the scalability of the platform on water boxes up to 7.7 million atoms using up to 68 V100 GPUs.

4 Performance and Scalability Results

4.1 Benchmark Systems

We use water boxes of increasing size as benchmark systems as well as some solvated proteins.^{10,11} The solvated proteins and their respective number of atoms, in parentheses, are: DHFR protein (23558), SARS-CoV2 Mpro protein (98500) and COX protein (174219). For the water boxes: 648 (i.e small), 4800 (big), 12000 (huge), 19200 (globe), 96000 (puddle), 288000 (pond), 864000 (lake), 2592000 (bay) and 7776000 (sea). After equilibration, we evaluated the performance on short NVE MD simulations.

4.2 GPU Performances

To ensure the performance and portability of our platform, we ran tests on different GPU infrastructures such as Tesla V100 nodes of the Jean-Zay supercomputer, the Irène Joliot Curie ATOS Sequana supercomputer V100 partition or a NVIDIA DGX A100. In the rest of the text the default device is the Tesla V100 if not mentioned otherwise. For each system, we performed 2.5 ps MD simulations

System/Model	ANI	AMOEBA	Hybrid
DHFR	19.42	9.08	5.16
COX	28.13	10.52	n/a

Table 1 Global Peak performance in percentage(%) assessed over a 50 femtoseconds MD trajectory. The Quadro GV100 was chosen to be the reference device.

with a Verlet integrator using a 0.5 fs time-step and average the performance over the complete runs. Figures 1 gather single GPU device performances.

Before discussing performance results let us introduce three critical concepts: saturation, utilization and peak performance. Saturation represents the ratio of resources used by the algorithm against the actual resources supplied by the GPU. It is closely related to the degree of parallelism expressed within the algorithm and its practical use in the simulation. Given the fact that recent *GPUs* provide and execute several thousands of threads at the same time to run calculations on numerous computational cores, complete saturation is naturally not achieved for small systems. On the other hand, the device utilization represents the percentage of execution time during which the *GPU* is active. As the *GPU* is driven by the *CPU*, its utilization heavily depends on both the *CPU* speed and the amount of code actually offloaded to the device. It is essential to rely on asynchronous computation and to develop a device-resident application in order to achieve a complete *GPU* utilization over time. Finally, peak performance (PP) describes how an algorithm asymptotically harnesses the computational power of the device on which it operates. Increasing this metric implies to maximize arithmetic operations over memory. However, one can only assess device peak performance in terms of floating points operations when both saturation and utilization are maximized. With a typical HPC device such as Quadro GV100 which delivers over 15.6 TFlop/s in single precision arithmetic (4 bytes), around 69 arithmetic operations can be performed between two consecutive float transactions from global memory, in order to reach the peak performance. Knowing this, we analyze the *GPU* peak performance of Deep-HP and Tinker-HP AMOEBA, in both separate and hybrid runs, using the reference GV100 Card. Results are depicted in Table 1. We can see the influence of device saturation on peak performance while running pure ML models, from the under-saturated DHFR system to the over-saturated COX one. MLPs manage to reach excellent peak performance on *GPU* platforms due to the large amount of calculations induced by the numerous matrix-vector products involved. For AMOEBA, on the other hand, the relatively tiny increase of peak performance for both systems - second column of tab 1 - denotes an excellent saturation and utilization of the device, regardless the size. The overall peak, however, reaches a lower 10.52%, which is still satisfactory given the complexity of the algorithm involved in the PFF calculation.

To study the complexity of the algorithm, we ran the benchmark systems on a single DGX A100 with two ANI models and compared the performance against the AMOEBA force field (see Figure 1a). The ANI-1ccx simulations are performed on water boxes ranging from 648 to 96000 atoms. For ANI-2x we also considered three solvated proteins: DHFR, SARS-CoV2 Mpro and COX. Furthermore, for these tests, we performed inference using only one instance from the ensemble of eight neural network predictors of the ANI models. On water boxes, ANI-1ccx is found to be between 2 and 7% faster than ANI-2x due to the models intrinsic complexities. Figure 1 a) shows the performance of both ANI-2x and AMOEBA. On the 648 and 4800 atoms systems, AMOEBA is 1.85 and 2.20 times faster than ANI respectively. On the first four water systems the ratio grows as $\mathcal{O}(N)$ with respect to the number of atoms N , with a Pearson coefficient equal to 0.995. On the protein systems the ratio still grows linearly but with a smaller slope: roughly a factor 2 is preserved.

To further analyze the computational bottleneck of HDNNP models, we evaluated the contribution of each of the model’s constituents to the overall execution time (Figure 1 SI). For small systems more than 40% of the cost is due to the gradients and AEV computations. The Tinker-HP neighbor list is less than 5% of the cost, demonstrating the performance of the implementation. For larger systems, the computational cost is largely dominated by the gradients computation (i.e. more than 50%). Thus, ML potentials computational performances are now mainly limited by back-propagation and not by the environment vector (the latter mainly being the memory bottleneck). Accelerating the gradients estimation will therefore be of the utmost importance for future implementations. Deep-HP also provides a keyword to automatically use mixed precision within PyTorch. The automatic mixed precision is using a combination of half and single precision operations without a severe loss on the model’s accuracy. It can theoretically deliver a 2-3 times performance boost, enabling faster gradients and NN evaluations by leveraging Tensor Cores, provided that the underlying model is large enough.

4.3 Multi-GPU Performance and Scalability of ANI Models within Tinker-HP

In the following, we assess and discuss the multi-node performance of Deep-HP. The Jean Zay HPE SGI 8600 *GPU* system holds numerous computing nodes accelerated by 4 interconnected Tesla V100 devices each. Ideally, a parallel algorithm associated to a certain amount of resources (N processors for instance), whose load is equally distributed across all resources, will exactly perform N times faster. Experimentally, an intermediate step, occupied with communications, affects the performance to a varying degree depending on size and pattern of these communications in comparison with the amount of calculations. When the number of allocated resources increases, global synchronizations induced by collective communications significantly slow down the parallel

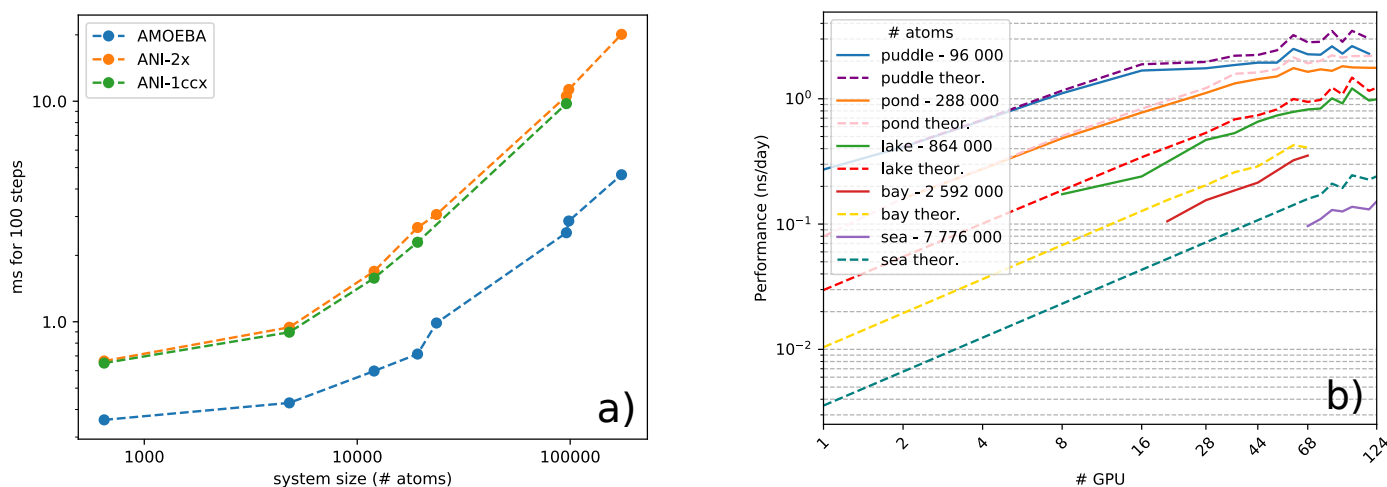


Figure 1 a) Performance comparison between ANI-1ccx(1NN), ANI-2x(1NN) and AMOEBA models in ms for 100 steps, over increasing system size, on a single Nvidia Tesla A100. b) Strong scaling logarithmic scale plot of ANI-2x model on benchmark systems. Simulations are performed in the NVE ensemble using a Verlet integrator and a 0.5 fs time-step.

execution and, therefore, impact the asymptotic behavior of the strong scalability. Communication patterns and speed are subsequently the principal obstacles to achieve an ideal scaling. In our case, the domain decomposition method coupled with ANI offers an up-bounded communication pattern, which allows to use several nodes without enduring severe performance loss too quickly, as it is the case with multi-node PFF on *GPUs*.¹¹ As displayed in Figure 1 b), we are able to scale up to 11 nodes (44 devices) for a 864000 atoms water box, before suffering from communication overheads and insufficient load. On the other hand, note that an accurate estimation of the gradients for each atom requires a complete knowledge of its surrounding environment up to a predetermined distance. The current implementation is however not optimal for a large number of processes and the performance starts to cap when half the minimum length of a domain equals the cutoff distance of the atomic environments. This is due to some redundancy between processes for the calculation of AEVs and energies of atoms from neighbouring domains. To illustrate this effect, we made an estimation of the performance in the case of no computational redundancy and plot it for every test case in dashed lines within Figure 1 b). As anticipated, dealing with this effect can offer a significant 40% boost in the parallel run as is observed for the sea water box. Thus, future implementations should address this issue in order to maximize multi-nodes performance.

4.4 Multi-timestep Integrator: RESPA/RESPA1

As accurate as the hybrid ANI/AMOEBA model can be, the stiff intramolecular interactions reproduced by the MLP limit the integration time-step to 0.2-0.3 fs, thus making the study of large proteins on long biological time scales a daunting task. One

way to speed up MD is to use larger time steps through multi-time-stepping (MTS) methods. Typical MTS schemes exploit the separability of the potential energy into a computationally expensive, slowly varying part and a cheap, quickly varying part, and use a specific integration scheme, RESPA⁵¹, that allows for less frequent evaluations of the expensive part. In particular in the context of the AMOEBA PFF, Tinker-*HP* uses either a bonded/non-bonded splitting or a three-stage separation between bonded, short-range non-bonded and long-range non-bonded interactions⁵² (denoted as RESPA1 in the rest of the text). In both cases, temperature control is made through a BAOAB discretization of a Langevin equation⁵³. In this context, the bonded forces are integrated using a small 0.2-0.3 fs time-step and the outermost time-step can be taken as 2 fs or 6 fs depending on the splitting. These can be further pushed by using Hydrogen Mass Repartitioning (HMR)^{52,54}. These integration schemes extend the applicability of PFFs to longer time-scale reducing the gap with classical FFs, as demonstrated with recent simulations of tens of μ s of the SARS-CoV2 protease².

Even though MLPs are much less expensive than *ab initio* calculations, the most common MLPs with feed-forward neural networks are still much more expensive than FFs, even polarizable ones. To reduce this gap and be able to simulate large biological systems, we combined our hybrid model with MTS integrators using the RESPA scheme. We assume that AMOEBA is a good approximation of the ML potential for the isolated solute so that their energy difference $\Delta V_{ML}(P) = V_{ML}(P) - V_{AMOEB}(P)$ should produce small forces that can be integrated using a larger time-step. This is done in the same spirit as in ref⁵⁵ in the context of accelerating *ab initio* molecular dynamics. We thus associate this difference with the non-bonded part of the AMOEBA model and

splits	0.2	0.25/1	0.25/2	0.25/2/4	0.25/2/6
Benzene	1.0	4.78	8.92	14.02	19.10
Water	1.0	4.34	8.29	-	-
Integrator-type	V	R	R	R1	R1(HMR)

Table 2 . Speedup of hybrid models with RESPA (R) and RESPA1 (R1) Integrators calculated with respect to Velocity-Verlet (V) 0.2 fs time step.

end up with the following separation:

$$V_{\text{HYB}}^{\text{fast}}(P \cup W) = V_{\text{AMOEB A}}^{\text{bond}}(P \cup W) \quad (8)$$

$$V_{\text{HYB}}^{\text{slow}}(P \cup W) = \Delta V_{\text{ML}}(P) + V_{\text{AMOEB A}}^{\text{nonbond}}(P \cup W) \quad (9)$$

where $V_{\text{HYB}}^{\text{fast}}$ is evaluated every inner time-step and $V_{\text{HYB}}^{\text{slow}}$ every outer one. In the RESPA1 framework, the potential energy difference $\Delta V_{\text{ML}}(P)$ is associated with the long range interactions and evaluated at the outermost time-step.

To assess the accuracy of each integrator we computed the solvation free energy of two systems as solute using the hybrid model described above with the ANI-2x version: the benzene molecule solvated in a cubic box of 996 water molecules with a 31 Å edge and a water molecule in a cubic box of 3999 other water molecules with a 49 Å edge. For each of these systems and integrators, we computed their solvation free energy by running 21 independent trajectories of 2 ns where the ligand is progressively decoupled from its water environment, first by annihilating its permanent multipoles and polarizabilities and then by scaling the associated van der Waals interactions (while using a softcore). The trajectories were run in the NPT ensemble at 300 K and 1 atmosphere using a Berendsen barostat and either a Bussi thermostat⁵⁶ (when velocity verlet is used) or a langevin one for the MTS simulations as mentioned previously. The free energy differences were then computed using the BAR method⁵⁷. Results were compared with a reference Velocity-Verlet integrator using a 0.2 fs time-step. The AMOEBA bonded forces were always evaluated every 0.25 fs. In the case of a bonded/non bonded split, the non bonded forces were evaluated either every 1 or 2 fs, and in the case where the non bonded forces are further split between short range and long range ones, the short-range non bonded forces were evaluated every 2 fs and the long range ones either every 4 fs or 6 fs. As explained above, the MLP forces are always computed at the outermost time-step. Table 2 shows the speedup of our hybrid model with various MTS setups compared to the reference Velocity Verlet with 0.2 fs time-step one. Overall, these schemes yield up to a more than 8 fold acceleration for the simpler split, and up to a 20 fold acceleration for the RESPA-1 split.

These integrators thus extend the applicability of machine learning-driven molecular dynamics to larger biologically-relevant systems and to longer-time-scale simulations. In practice, the resulting performance gain helps reduce the computational gap between ab-initio machine learning potential and force

fields as can be seen in table 2 of SI.

4.5 Solvation Free Energies

4.5.1 Computational Details

To assess the performance of the ANI/AMOEB A hybrid model, we computed the associated solvation free energies of small molecules within non aqueous and aqueous conditions as done in references^{58,59}. The solvents considered (with their dielectric permittivity) are: Toluene ($\epsilon = 2.38$), Acetonitrile ($\epsilon = 36.64$), DMSO ($\epsilon = 47.24$) and water ($\epsilon = 77.16$). The description of the solutes can be found in SI. Solvation free energies in water have been intensively studied as they are an essential tool to drive drug design efforts and to test the validity of various computational methods and models^{4,60}. However, the polarizability, and thus the dielectric constant, of an environment can change during biological processes, for instance at the interface between protein-ligands, intra-molecular interactions and the passing through cell membranes which justifies the computation of solvation free energies with these various solvents. The results are compared with experimental data and with the AMOEBA ones.

We withdrew molecules from the datasets that have chemical elements not available in ANI-2x. This led us to a total of 39 molecules solvated in water from reference³³, 20 molecules solvated in toluene, 6 in acetonitrile and 6 in DMSO from J. Essex et al.⁵⁸. All the systems were prepared following standard equilibration protocol: after a geometry optimization, they were progressively heated up to 300 K in NVT and then equilibrated for 1 ns in the NPT ensemble at the same temperature and 1 atmosphere. In all cases, we used the most simple multiple time-step integrator presented above with a 0.25 fs time-step for bonded terms and 1 fs for the outermost one. The Bussi thermostat and the Berendsen barostat were used. The Van der Waals interactions cutoff was chosen at 12 Å and the electrostatic interactions were handled with the smooth particle mesh ewald method³⁴ with a 7 Å real space cutoff and default Tinker-HP grid size. We used the same scheme as before to decouple the systems from their environment with 21 independent windows of 2 ns.

4.5.2 Results and Discussion

The experimental, AMOEBA and ANI/AMOEB A solvation free energies data are provided in SI (see Tables S1–S4). In the less polar solvent, Toluene ($\epsilon = 2.38$), AMOEBA results appear very similar to the hybrid ANI/AMOEB A ones, with a respective

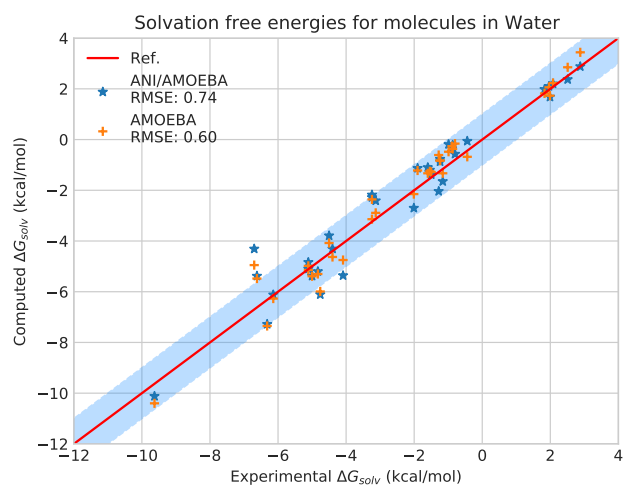
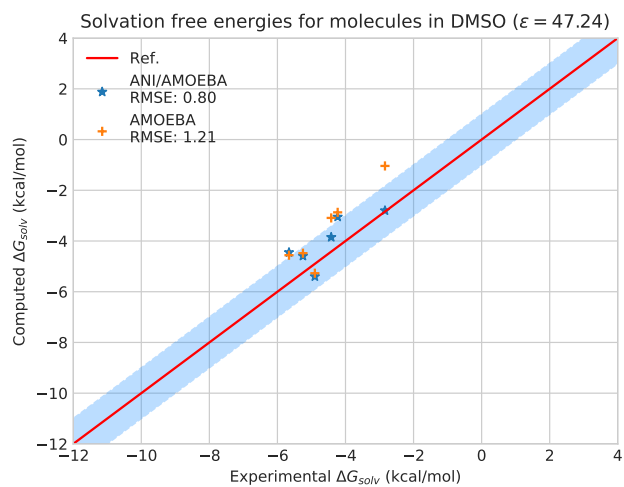
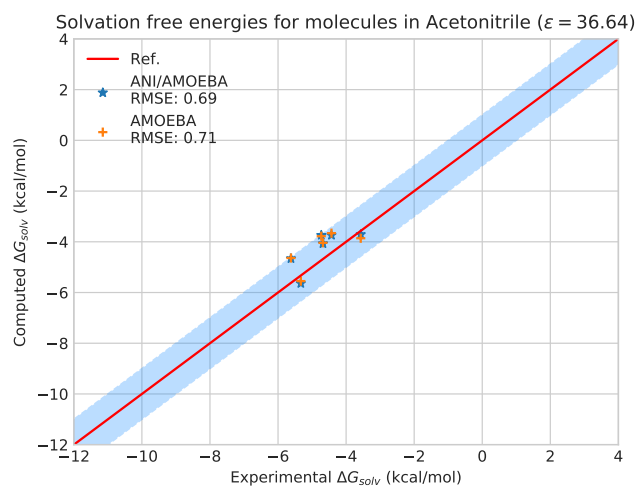
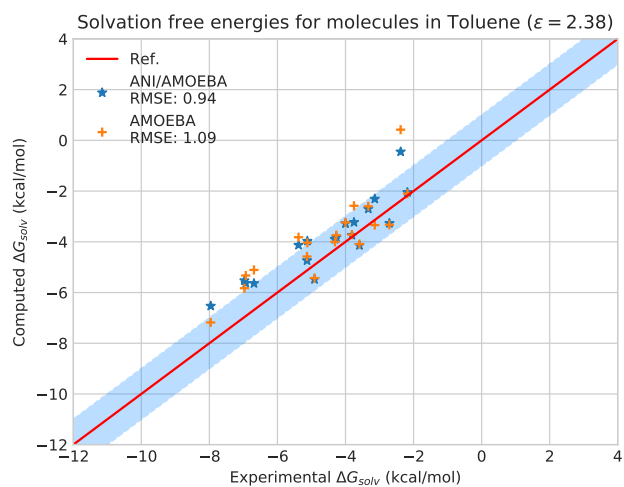


Figure 2 Solvation free energies of molecules in different solvents computed with AMOEBA (orange) from refs^{58,59} versus hybrid model ANI/AMOEBA (blue) and experiment (red). The blue domain correspond to the so-called chemical accuracy: error of 1 kcal/mol w.r.t experiment.

RMSE of 1.06 kcal/mol vs 1.09 kcal/mol. However, this is mainly due to 2 outliers that have an error greater than 1.5 kcal/mol with experiment, especially the methylamine for which AMOEBA exhibits a 0.23 kcal/mol error while ANI/AMOEBA culminates at 2.60 kcal/mol. By removing the methylamine compound, ANI/AMOEBA accuracy slightly outperforms AMOEBA as the RMSE becomes respectively 0.93 kcal/mol vs 1.09 kcal/mol. In Acetonitrile, ANI/AMOEBA is shown to perform slightly better than AMOEBA by 0.02 kcal/mol. Strikingly, in the DMSO, ANI/AMOEBA performs much better than AMOEBA, with a respective RMSE of 0.80 kcal/mol vs 1.21 kcal/mol. In water, the hybrid model performs slightly worse than AMOEBA with a RMSE of 0.86 kcal/mol vs 0.59 kcal/mol for AMOEBA. However, this is again due to two "amine" outliers (methylamine and dimethylamine). Removing them leads to a RMSE decrease to 0.76 kcal for the hybrid model while AMOEBA remains roughly identical. Overall, the hybrid ANI/AMOEBA approach benefits from the inclusion of the neural network and appears to be more accurate than AMOEBA for three out of the four studied solvents: Toluene, Acetonitrile and DMSO. In contrast, AMOEBA is more accurate in the most polar solvent: ie. water. This result is not surprising as the AMOEBA water model is well-known for its accuracy and capabilities to reproduce numerous water-related experimental data²⁸. Note that part of the discussed errors may still arise from insufficient sampling beside the models' intrinsic errors.^{61,62} Indeed, 5 ns of simulations by window were performed for the AMOEBA reference while only 2 ns were performed for ANI/AMOEBA. In contrast with the results obtained by Rowley et al⁶³ that show the difficulties of the ANI-2x potential for modeling charged systems within a hybrid approach with non-polarizable force fields we observed accurate results even for charged systems. For example, the hybrid approach yields good results for nitromethane, which is globally neutral but still bears two charged groups. The main issue observed in our new ANI/AMOEBA approach is clearly linked to some present identified limitations of the ANI-2x potential, such as the amine groups. Finally, one can point out that the total simulation length performed on the discussed 80 molecules goes beyond 4 μ s, highlighting the capabilities of the Deep-HP neural network platform. To date, this is among the longest simulations with such models and direct application to practical systems. In the next section, we go a step further in terms of complexity and report the hybrid model performance on 13 host-guest systems taken from the SAMPL competitions.⁶⁴

4.6 Host-guest Binding Free Energies: SAMPL Challenges

4.6.1 Computational details

The absolute binding free energy values of 12 guests from the SAMPL4 CB[7]-guest challenge⁶⁵ and the G9 guest of the SAMPL6 cucurbit[8]uril host-guest challenge were calculated

with the hybrid ANI/AMOEBA model as the difference between the free energy of decoupling the ligands within the host and in solution. The optimized structures and parameters for the AMOEBA FF were taken from literature.⁶⁵⁻⁶⁸ Same protocol as before was used except that the RESPA outer time-step was changed from 1 fs to 2 fs which still give a satisfactory accuracy as can be seen in Table 1 of SI.

4.6.2 Results and Discussion

The binding free energies of the host-guest systems are depicted in Figure 3 and in SI (see Table S6) and reference AMOEBA values were taken from^{65,68}. First, it is important to notice that most of the ligands encompass a net charge of 1 or 2. Only a single neutral host-guest system extracted from the SAMPL6 challenge is present. Overall, the hybrid ANI/AMOEBA gives slightly better results than AMOEBA. While the sampling may have an impact, the hybrid ANI/AMOEBA performance is by itself satisfactory as ANI was not designed for modeling ionic species as stated above. ANI/AMOEBA even largely outperforms AMOEBA for the two net charged guest ligands C1, C5b. One explanation could be that the initial discrepancy of ANI is compensated by AMOEBA through the inclusion of long-range interactions (electrostatics and many-body polarization). For both models, the worst agreement with the experience is found to be associated to C5. Ren et al.,⁶⁷ showed that this discrepancy was already known and comes from a lack of sampling that requires the use of enhanced sampling techniques such as orthogonal space random walk⁶⁹. ANI/AMOEBA exhibits larger error than AMOEBA on the C7 and C8 guest ligands which are associated to high enthalpy changes throughout binding. Their changes of enthalpy can be traced back to some gains in term of H-bond interactions from solution to the host-guest complex, suggesting that improvements of ANI-2x towards improved H-bond treatment could be beneficial. Overall, despite the discussed potential drawbacks, the ANI/AMOEBA hybrid model shows a greater accuracy than AMOEBA alone on a variety of host-guest systems. This flexibility and stability of the potential benefits from the MLP combination with AMOEBA's long-range effects that are not taken into account in MLP.

It also benefits from the fact that some MLP limitations (inclusion of counter ions etc.) are not an issue anymore thanks to AMOEBA in the hybrid framework enabling therefore to perform real periodic boundary simulations including a full neural network. It is worth reporting that on the neutral SAMPL8 host-guest system, the ANI/AMOEBA results almost exactly match experiment.

Overall the hybrid ANI/AMOEBA model is in very good agreement with experimental results and can accurately predict binding free energies of flexible charged systems.

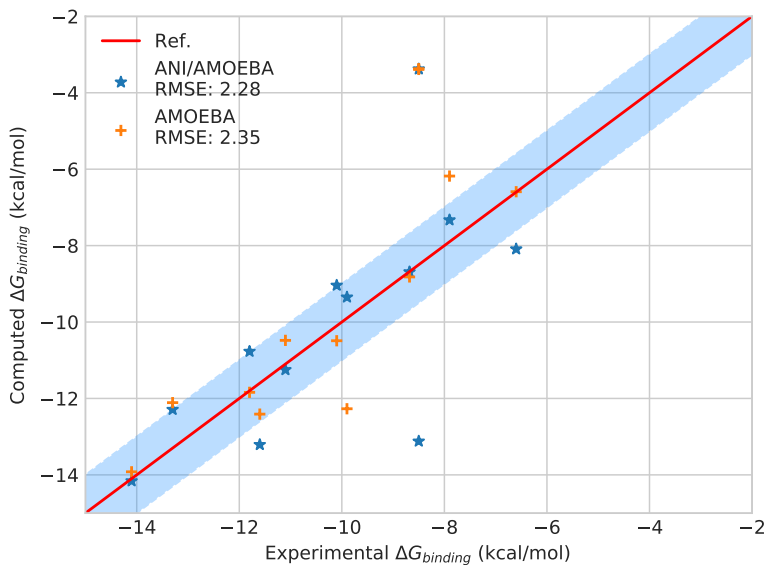


Figure 3 Binding free energies of host-guest systems of the SAMPL4 and SAMPL8 blind challenges with AMOEBA (orange) from refs⁶⁵ versus hybrid model ANI/AMOEBA (blue) and experimental (red). The blue domain correspond to the so-called chemical accuracy: error of 1 kcal/mol w.r.t experiment.

5 Conclusion and Perspectives

We first introduced Deep-HP, a massively parallel multi-GPU neural network platform which is a new component of the Tinker-HP software. The platform allows the coupling of state-of-the-art polarizable force fields with any ML potential. The platform capabilities have been demonstrated by simulating large biologically-relevant systems on more than 124 GPUs.

We then developed a hybrid Deep Neural Networks/Polarizable potential that uses the ANI-2x ML potential for the solute-solute interactions and AMOEBA for the rest. The development of the hybrid potential was motivated by the difficulty to model modelling water-solute as well as water-water interactions, a task that is presently better achieved by PFFs. On the opposite, neural networks are better able to capture complex intramolecular interactions at an accuracy reaching the CCSDT(T) gold standard of computational chemistry. In addition to intramolecular interactions, NNPs also provide a route towards reactivity without the need of complex reactive force field parametrization.

We extended our hybrid model computational capabilities by designing RESPA and RESPA1-like multi-timestep integrators that can speedup up simulation up to a 20-fold with respect to Velocity Verlet 0.2fs. In that context, the relative speedup of AMOEBA compared the hybrid ANI/AMOEBA dropped from 40 to 2. The hybrid approach offers the inclusion of long-range effects (electrostatics and many-body polarization) and the capability to perform accurate simulations that include polarizable counter ions.

The combination of these approaches opens the door to accurate routine long timescale simulations using NNPs, up to million of atoms on biological systems.

Our hybrid model accuracy was first assessed on solvation free energies of 80 molecules, with a large panel of functional groups, within four aqueous and non-aqueous solvents. The hybrid model tends to outperform AMOEBA accuracy on the non-aqueous solvents while performing well in water too opening a path towards the simulation of complex biological processes for which the polarizability of the environment is important.^{3,70}

We then reported the performance of our model on binding free energies of 13 host-guest challenging systems taken from the SAMPL host-guest binding competitions. Although most of ligands are charged, our hybrid model outperforms AMOEBA's accuracy despite the complex chemical environments.

Overall, the Deep-HP platform, which takes advantage of state-of-the-art Tinker-HP GPU code, was able to produce within a few days 6 μ s of hybrid NNPS/PFFs simulations. For example, computing a binding free energy takes only about 10 hours on a common GPU card. Such performances should continue to improve thanks to further optimizations, further TorchANI updates and GPUs hardware evolutions. One key aspect of such GPU-accelerated platform is to enable the integration of machine learning potentials while also including the polarizable force fields many-body effects and long-range physics-based corrections. In this line, our hybrid framework will allow for the implementation

of the next generation of MLPs that should be able to gradually fix their present limitations and will be a place for their further development. It includes direct neural networks coupling with physics-driven contributions going beyond multipolar electrostatics and polarization through inclusion of many-body dispersion models.^{71,72} As Deep-HP's purpose is to push a trained ML/hybrid model towards large scale production simulations, we expect extensions of the present simulation capabilities to other class of systems towards materials and catalysis applications. Overall, the present ANI/AMOEBA hybrid model goes a step further towards the grail of molecular mechanics which is the unification within a many-body interaction potential of the short-range quantum mechanical accuracy and of the physically motivated long-range effects at force field cost.

Author contributions statement

T. J.I, O. A and T. P performed simulations;
O. A, O. I, T. J.I, L. L and T. P contributed new code;
L. L, O. I, T. J.I, P. R., T. P, J-P. P contributed new methodology;
T. J.I, L. L., P. R., J-P. P contributed analytical tool;
T. J.I, L. L, O. I, P. R., H. G, J-P. P analyzed data.
T. J.I, L. L, T. P, H. G, O. I and J-P. P wrote the paper;
J-P. P designed the research.

Code availability

Tinker-HP is freely accessible to Academics via GitHub : <https://github.com/TinkerTools/tinker-hp>

Conflicts of interest

There are no conflicts to declare.

Acknowledgements

This work has received funding from the European Research Council (ERC) under the European Union's Horizon 2020 research and innovation program (grant agreement No 810367), project EMC2 (JPP). Simulations have been performed at GENCI on the Jean Zay machine (IDRIS, Orsay, France) on grant no A0070707671 and at TGCC (Bruyères le Châtel, France) on the Irène Joliot Curie machine. The work performed by H.G. and O.I. (PI) was made possible by the Office of Naval Research (ONR) through support provided by the Energetic Materials Program (MURI grant no. N00014-21-1-2476). This research is part of the Frontera computing project at the Texas Advanced Computing Center. Frontera is made possible by the National Science Foundation award OAC-1818253.

References

- 1 J. Jumper, R. Evans, A. Pritzel, T. Green, M. Figurnov, O. Ronneberger, K. Tunyasuvunakool, R. Bates, A. Žídek, A. Potapenko, A. Bridgland, C. Meyer, S. A. A. Kohl, A. J. Ballard, A. Cowie, B. Romera-Paredes, S. Nikolov, R. Jain, J. Adler, T. Back, S. Petersen, D. Reiman, E. Clancy, M. Zielinski, M. Steinegger, M. Pacholska, T. Berghammer, S. Boden-stein, D. Silver, O. Vinyals, A. W. Senior, K. Kavukcuoglu, P. Kohli and D. Hassabis, *Nature*, 2021, **596**, 583–589.
- 2 T. Jaffrelot Inizan, F. Célerse, O. Adjoua, D. El Ahdab, L.-H. Jolly, C. Liu, P. Ren, M. Montes, N. Lagarde, L. Lagardère, P. Monmarché and J.-P. Piquemal, *Chem. Sci.*, 2021, **12**, 4889–4907.
- 3 D. El Ahdab, L. Lagardère, T. J. Inizan, F. Célerse, C. Liu, O. Adjoua, L.-H. Jolly, N. Gresh, Z. Hobaika, P. Ren, R. G. Maroun and J.-P. Piquemal, *The Journal of Physical Chemistry Letters*, 2021, **12**, 6218–6226.
- 4 L. El Khoury, Z. Jing, A. Cuzzolin, A. Deplano, D. Loco, B. Sattarov, F. Hédin, S. Wendeborn, C. Ho, D. El Ahdab, T. Jaffrelot Inizan, M. Sturlese, A. Susic, M. Volpiana, A. Lugato, M. Barone, B. Gatto, M. L. Macchia, M. Bellanda, R. Battistutta, C. Salata, I. Kondratov, R. Iminov, A. Khairulin, Y. Mykhalonok, A. Pochevko, V. Chashka-Ratushnyi, I. Kos, S. Moro, M. Montes, P. Ren, J. W. Ponder, L. Lagardère, J.-P. Piquemal and D. Sabbadin, *Chem. Sci.*, 2022, **13**, 3674–3687.
- 5 N. Gresh, G. A. Cisneros, T. A. Darden and J.-P. Piquemal, *J. Chem. Theory Comput.*, 2007, **3**, 1960–1986.
- 6 S. Naseem-Khan, L. Lagardère, C. Narth, G. A. Cisneros, P. Ren, N. Gresh and J.-P. Piquemal, *Journal of Chemical Theory and Computation*, 2022, **18**, 3607–3621.
- 7 J. Melcr and J.-P. Piquemal, *Frontiers in Molecular Biosciences*, 2019, **6**, 143.
- 8 Y. Shi, P. Ren, M. Schnieders and J.-P. Piquemal, in *Polarizable Force Fields for Biomolecular Modeling*, John Wiley and Sons, Ltd, 2015, ch. 2, pp. 51–86.
- 9 Z. Jing, C. Liu, S. Y. Cheng, R. Qi, B. D. Walker, J.-P. Piquemal and P. Ren, *Annual Review of Biophysics*, 2019, **48**, 371–394.
- 10 L. Lagardère, L.-H. Jolly, F. Lipparini, F. Aviat, B. Stamm, Z. F. Jing, M. Harger, H. Torabifard, G. A. Cisneros, M. J. Schnieders, N. Gresh, Y. Maday, P. Y. Ren, J. W. Ponder and J.-P. Piquemal, *Chem. Sci.*, 2018, **9**, 956–972.
- 11 O. Adjoua, L. Lagardère, L.-H. Jolly, A. Durocher, T. Very, I. Dupays, Z. Wang, T. J. Inizan, F. Célerse, P. Ren, J. W. Ponder and J.-P. Piquemal, *Journal of Chemical Theory and Computation*, 2021, **17**, 2034–2053.
- 12 A. P. Bartók, M. C. Payne, R. Kondor and G. Csányi, *Phys. Rev. Lett.*, 2010, **104**, 136403.
- 13 A. Thompson, L. Swiler, C. Trott, S. Foiles and G. Tucker, *J. Comput. Phys.*, 2015, **285**, 316–330.

- 14 V. Vovk, in *Kernel Ridge Regression*, ed. B. Schölkopf, Z. Luo and V. Vovk, Springer Berlin Heidelberg, Berlin, Heidelberg, 2013, pp. 105–116.
- 15 H. E. Saucedo, S. Chmiela, I. Poltavsky, K.-R. Müller and A. Tkatchenko, *The Journal of Chemical Physics*, 2019, **150**, 114102.
- 16 S. Chmiela, A. Tkatchenko, H. E. Saucedo, I. Poltavsky, K. T. Schütt and K.-R. Müller, *Science Advances*, 2017, **3**, e1603015.
- 17 S. Chmiela, H. E. Saucedo, K.-R. Müller and A. Tkatchenko, *Nature Communications*, 2018, **9**, 3887.
- 18 H. E. Saucedo, S. Chmiela, I. Poltavsky, K.-R. Müller and A. Tkatchenko, *The Journal of Chemical Physics*, 2019, **150**, 114102.
- 19 O. Ivanciuc, in *Applications of Support Vector Machines in Chemistry*, John Wiley and Sons, Ltd, 2007, ch. 6, pp. 291–400.
- 20 A. P. Bartók, R. Kondor and G. Csányi, *Phys. Rev. B*, 2013, **87**, 184115.
- 21 A. Fabrizio, K. R. Briling and C. Corminboeuf, *Digital Discovery*, 2022, –.
- 22 J. Behler and M. Parrinello, *Phys. Rev. Lett.*, 2007, **98**, 146401.
- 23 M. Gastegger, L. Schwiedrzik, M. Bittermann, F. Berzsényi and P. Marquetand, *The Journal of Chemical Physics*, 2018, **148**, 241709.
- 24 J. Behler, *Chemical Reviews*, 2021, **121**, 10037–10072.
- 25 J. S. Smith, O. Isayev and A. E. Roitberg, *Chem. Sci.*, 2017, **8**, 3192–3203.
- 26 W. Jia, H. Wang, M. Chen, D. Lu, L. Lin, R. Car, W. E and L. Zhang, Proceedings of the International Conference for High Performance Computing, Networking, Storage and Analysis, 2020.
- 27 T. W. Ko, J. A. Finkler, S. Goedecker and J. Behler, *Nature Communications*, 2021, **12**, 398.
- 28 P. Ren and J. W. Ponder, *The Journal of Physical Chemistry B*, 2003, **107**, 5933–5947.
- 29 J. W. Ponder, C. Wu, P. Ren, V. S. Pande, J. D. Chodera, M. J. Schnieders, I. Haque, D. L. Mobley, D. S. Lambrecht, R. A. DiStasio, M. Head-Gordon, G. N. I. Clark, M. E. Johnson and T. Head-Gordon, *The Journal of Physical Chemistry B*, 2010, **114**, 2549–2564.
- 30 N. L. Allinger, Y. H. Yuh and J. H. Lii, *Journal of the American Chemical Society*, 1989, **111**, 8551–8566.
- 31 B. T. Thole, *Chemical Physics*, 1981, **59**, 341–350.
- 32 T. A. Halgren, *Journal of the American Chemical Society*, 1992, **114**, 7827–7843.
- 33 B. Walker, C. Liu, E. Wait and P. Ren, *Journal of Computational Chemistry*, 2022, **n/a**.
- 34 U. Essmann, L. Perera, M. L. Berkowitz, T. Darden, H. Lee and L. G. Pedersen, *The Journal of Chemical Physics*, 1995, **103**, 8577–8593.
- 35 L. Lagardère, F. Lipparini, E. Polack, B. Stamm, E. Cancès, M. Schnieders, P. Ren, Y. Maday and J.-P. Piquemal, *Journal of chemical theory and computation*, 2015, **11**, 2589–2599.
- 36 J. W. Ponder, C. Wu, P. Ren, V. S. Pande, J. D. Chodera, M. J. Schnieders, I. Haque, D. L. Mobley, D. S. Lambrecht, R. A. DiStasio Jr et al., *J. Phys. Chem. B.*, 2010, **114**, 2549–2564.
- 37 A. Grossfield, P. Ren and J. W. Ponder, *Journal of the American Chemical Society*, 2003, **125**, 15671–15682.
- 38 J. C. Wu, J.-P. Piquemal, R. Chaudret, P. Reinhardt and P. Ren, *Journal of Chemical Theory and Computation*, 2010, **6**, 2059–2070.
- 39 Y. Shi, Z. Xia, J. Zhang, R. Best, C. Wu, J. W. Ponder and P. Ren, *J. Chem. Theory. Comput.*, 2013, **9**, 4046–4063.
- 40 C. Zhang, C. Lu, Z. Jing, C. Wu, J.-P. Piquemal, J. W. Ponder and P. Ren, *Journal of Chemical Theory and Computation*, 2018, **14**, 2084–2108.
- 41 J. S. Smith, B. Nebgen, N. Lubbers, O. Isayev and A. E. Roitberg, *The Journal of Chemical Physics*, 2018, **148**, 241733.
- 42 J. S. Smith, O. Isayev and A. E. Roitberg, *Scientific Data*, 2017, **4**, 170193.
- 43 J. S. Smith, R. Zubatyuk, B. Nebgen, N. Lubbers, K. Barros, A. E. Roitberg, O. Isayev and S. Tretiak, *Scientific Data*, 2020, **7**, 134.
- 44 C. Devereux, J. S. Smith, K. K. Huddleston, K. Barros, R. Zubatyuk, O. Isayev and A. E. Roitberg, *Journal of Chemical Theory and Computation*, 2020, **16**, 4192–4202.
- 45 L. Zhang, J. Han, H. Wang, R. Car and W. E, *Phys. Rev. Lett.*, 2018, **120**, 143001.
- 46 H. Wang, L. Zhang, J. Han and W. E, *Computer Physics Communications*, 2018, **228**, 178–184.

- 47 J. Norberg and L. Nilsson, *Biophysical journal*, 2000, **79**, 1537–1553.
- 48 A. Paszke, S. Gross, F. Massa, A. Lerer, J. Bradbury, G. Chanan, T. Killeen, Z. Lin, N. Gimelshein, L. Antiga, A. Desmaison, A. Kopf, E. Yang, Z. DeVito, M. Raison, A. Tejani, S. Chilamkurthy, B. Steiner, L. Fang, J. Bai and S. Chintala, *Advances in Neural Information Processing Systems 32*, Curran Associates, Inc., 2019, pp. 8024–8035.
- 49 M. Abadi, A. Agarwal, P. Barham, E. Brevdo, Z. Chen, C. Citro, G. S. Corrado, A. Davis, J. Dean, M. Devin, S. Ghemawat, I. Goodfellow, A. Harp, G. Irving, M. Isard, Y. Jia, R. Jozefowicz, L. Kaiser, M. Kudlur, J. Levenberg, D. Mané, R. Monga, S. Moore, D. Murray, C. Olah, M. Schuster, J. Shlens, B. Steiner, I. Sutskever, K. Talwar, P. Tucker, V. Vanhoucke, V. Vasudevan, F. Viégas, O. Vinyals, P. Warden, M. Wattenberg, M. Wicke, Y. Yu and X. Zheng, *TensorFlow: Large-Scale Machine Learning on Heterogeneous Systems*, 2015, <https://www.tensorflow.org/>, Software available from tensorflow.org.
- 50 F. Chollet *et al.*, *Keras*, 2015, <https://github.com/fchollet/keras>.
- 51 M. Tuckerman, B. Berne and G. Martyna, *Journal of Chemical Physics*, 1992, **97**, 1990–2001.
- 52 L. Lagardère, F. Aviat and J.-P. Piquemal, *The Journal of Physical Chemistry Letters*, 2019, **10**, 2593–2599.
- 53 B. Leimkuhler and C. Matthews, *The Journal of chemical physics*, 2013, **138**, 05B601_1.
- 54 R. Zhou, E. Harder, H. Xu and B. J. Berne, *The Journal of Chemical Physics*, 2001, **115**, 2348–2358.
- 55 E. Liberatore, R. Meli and U. Rothlisberger, *Journal of chemical theory and computation*, 2018, **14**, 2834–2842.
- 56 G. Bussi, D. Donadio and M. Parrinello, *The Journal of chemical physics*, 2007, **126**, 014101.
- 57 C. H. Bennett, *Journal of Computational Physics*, 1976, **22**, 245–268.
- 58 N. A. Mohamed, R. T. Bradshaw and J. W. Essex, *Journal of Computational Chemistry*, 2016, **37**, 2749–2758.
- 59 J. C. Wu, G. Chattree and P. Ren, *Theoretical Chemistry Accounts*, 2012, **131**, 1138.
- 60 M. M. Ghahremanpour, J. Tirado-Rives, M. Deshmukh, J. A. Ippolito, C.-H. Zhang, I. Cabeza de Vaca, M.-E. Liosi, K. S. Anderson and W. L. Jorgensen, *ACS Medicinal Chemistry Letters*, 2020, **11**, 2526–2533.
- 61 Y. Miao, V. A. Feher and J. A. McCammon, *Journal of Chemical Theory and Computation*, 2015, **11**, 3584–3595.
- 62 F. Célerse, T. J. Inizan, L. Lagardère, O. Adjoua, P. Monmarché, Y. Miao, E. Derat and J.-P. Piquemal, *Journal of Chemical Theory and Computation*, 2022, **18**, 968–977.
- 63 S.-L. J. Lahey and C. N. Rowley, *Chem. Sci.*, 2020, **11**, 2362–2368.
- 64 M. Amezcua, L. El Khoury and D. L. Mobley, *Journal of Computer-Aided Molecular Design*, 2021, **35**, 1–35.
- 65 D. R. Bell, R. Qi, Z. Jing, J. Y. Xiang, C. Mejias, M. J. Schnieders, J. W. Ponder and P. Ren, *Phys. Chem. Chem. Phys.*, 2016, **18**, 30261–30269.
- 66 M. Harger, D. Li, Z. Wang, K. Dalby, L. Lagardère, J.-P. Piquemal, J. Ponder and P. Ren, *Journal of Computational Chemistry*, 2017, **38**, 2047–2055.
- 67 H. S. Muddana, A. T. Fenley, D. L. Mobley and M. K. Gilson, *Journal of Computer-Aided Molecular Design*, 2014, **28**, 305–317.
- 68 M. L. Laury, Z. Wang, A. S. Gordon and J. W. Ponder, *Journal of computer-aided molecular design*, 2018, **32**, 1087–1095.
- 69 J. R. Abella, S. Y. Cheng, Q. Wang, W. Yang and P. Ren, *Journal of chemical theory and computation*, 2014, **10**, 2792–2801.
- 70 T. Jaffrelot Inizan, F. Célerse, O. Adjoua, D. El Ahdab, L.-H. Jolly, C. Liu, P. Ren, M. Montes, N. Lagarde, L. Lagardère, P. Monmarché and J.-P. Piquemal, *Chem. Sci.*, 2021, **12**, 4889–4907.
- 71 P. P. Poier, L. Lagardère and J.-P. Piquemal, *Journal of Chemical Theory and Computation*, 2022, **18**, 1633–1645.
- 72 P. P. Poier, T. Jaffrelot Inizan, O. Adjoua, L. Lagardère and J.-P. Piquemal, *The Journal of Physical Chemistry Letters*, 2022, **13**, 4381–4388.